Quality Analysis of High-Frequency Air-Gun Shot Seismic Recordings in the Juan de Fuca Plate

by Sampath Rathnayaka and Haiying Gao

ABSTRACT

The goal of this study is to extract high-frequency seismic waveforms recorded by both offshore and onshore instrumentations and to quantitatively evaluate the data quality in terms of source-to-receiver distance, source parameters, water depth, and sediment thickness. There were two active-source seismic experiments within the Juan de Fuca plate, MGL1211 and MGL1212, during the first year deployment of the Cascadia Initiative Amphibious Array. In total, we chose 114 ocean-bottom seismometers and 211 inland stations located around the experiment region. The common receiver gathering analysis shows that most offshore stations located in deep-water record clear first *P*-wave arrivals up to 150 km away from the air-gun shot. The first arrival transits from crustal phase *Pg* to head wave *Pn* at a source-to-receiver distance of 25–40 km. For stations located at shallow water, the seismic recordings appear much noisier compared with those of deep-water stations. Only five inland stations record clear air-gun shot signals up to 200 km away from the source. The signal-to-noise ratio of the first *P* arrivals generally decreases from a few hundred down to a single number with increasing source-to-receiver distance, from deep (~3000 m) to shallow water (~100 m), with increasing sediment thickness and decreasing air-gun shot spacing and time interval. On average, the ratio appears 5–10 times lower at inland stations than at offshore stations. The sediment thickness estimated in this study demonstrates significant along-strike variations, which is up to 5 km offshore Oregon and 3.5 km offshore Washington. The coincidence of thick sediments with seismicity suggests the importance of sediments on the coupling of the plate interface.

Electronic Supplement: Tables that summarize the information of two active-source seismic experiments, types of instrumentations, and estimate of sediment thickness and figures showing the station locations, examples of air-gun shot recordings, distribution of signal-to-noise ratios for onshore stations, manual picks of the first *P*-wave arrivals (*Pn*), and distribution of sediment thickness, as well as comparison of sediment estimate from this study with other literatures.

INTRODUCTION

The Juan de Fuca (JdF) plate is subducting beneath the North American continent along the Cascadia subduction zone, western North America, at a rate of 3–4 cm/yr (e.g., McCaffrey *et al.*, 2007). Cascadia is under the threat of potential megathrust earthquakes and tsunamis in the near future (e.g., Wang and Trehu, 2016). The location and magnitude of subduction earthquakes are strongly influenced by the physical properties of the plate interface, subduction zone parameters, and rheology of the crust and upper mantle (e.g., Bilek, 2009; Wallace *et al.*, 2010). It has been suggested that at sediment-rich subduction zones such as Cascadia and Eastern Aleutian, sediment thickness and influx play a significant role in the observed along-strike variations of fault-slip behaviors (e.g., Song and Simons, 2003; Wells *et al.*, 2003; Wang and Trehu, 2016; Han *et al.*, 2017). A recent study by Phrampus *et al.* (2017) showed that sediment thickening along the accretionary wedge has a crucial effect on the thermal structure of the Cascadia subduction system. It was suggested that accumulation of overconsolidated sediments offshore the Washington margin contributes to the megathrust slip behavior and deformation of the accretionary wedge (Han *et al.*, 2017). Thick sediments within the accretionary wedge can also significantly amplify and extend durations of seismic surface waves (Guo *et al.*, 2016; Johnson *et al.*, 2017).

The active-source seismic reflection and refraction experiments have been successfully applied to study sedimentary, crustal, and upper-mantle structure and have provided high-resolution distribution of marine sediments along 2D profiles or within a relatively small region (e.g., Funck *et al.*, 2000; Bleibinhaus *et al.*, 2007; Shillington *et al.*, 2008; Dash and Spence, 2011; Trehu *et al.*, 2012; Christeson *et al.*, 2013). Recent active-source seismic experiments in Cascadia demonstrated that the sediment thickness increases from the JdF ridge toward the trench (Han *et al.*, 2016, 2017; Horning *et al.*, 2016). Along the Cascadia deformation front, the sediment thickness is relatively uniform on the seaside, which is about 2.5–3.0 km thick (Canales *et al.*, 2017). The sediments reach a maximum

doi: 10.1785/0220180274

thickness of up to 5 km within the accretionary wedge (Han *et al.*, 2017). The *P*-wave seismic velocity within the sediments varies within a range of 1.5–4.8 km/s, which increases with the increasing sediment thickness (Canales *et al.*, 2017; Han *et al.*, 2017). However, because of the lack of dense coverage of high-frequency seismic datasets, none of those previous studies were capable of resolving a 3D distribution of the sediment thickness within the JdF plate.

With the operation of the Cascadia Initiative seismic array from 2011 to 2015, a few studies provided 3D sediment distributions within the JdF and Gorda plates. With the ratio of vertical displacement to pressure of Rayleigh waves, Ruan *et al.* (2014) and Bell *et al.* (2015) found that the shear velocity of abyssal plain sediments varies at 0.1–1.0 km/s within a layer thickness of 0.1–1.4 km from the ridge to the deformation front, which correspondingly results in a shear-wave delay of 0.5–2.0 s. The estimates by Ruan *et al.* (2014) and Bell *et al.* (2015) revealed relatively thinner sediments compared with the active-source results by Han *et al.* (2016) and Horning *et al.* (2016). Gomberg (2018) extracted the sediment thickness from the velocity model by Stephenson (2007), which corresponds to the $V_P = 4.5$ km/s depth boundary. The sediment distribution shows an abrupt west–east thickening across the deformation front and demonstrates distinct along-strike variations within the accretionary wedge (Gomberg, 2018). In comparison with the results by Bell *et al.* (2015), the sediment by Gomberg (2018) is on average about 0.5 km thinner within the JdF plate.

In this study, we analyze high-frequency seismic waveforms from two active-source experiments within the JdF plate and evaluate the data quality. Our analysis shows that the quality of the air-gun shot recordings varies from deep to shallow water and from offshore to onshore. We provide a 3D distribution of the sediment thickness, extending from the ridge to the continental margin within the entire JdF plate.

EXTRACTION OF HIGH-FREQUENCY WAVEFORMS

Two active-source seismic experiments MGL1211 (Juan de Fuca plate: Ridge to trench) and MGL1212 (Cascadia Open-Access Seismic Transects) were carried out in June–July 2012, within the oceanic JdF plate (see seismic lines in Fig. 1 and Ⓔ Fig. S1, available in the electronic supplement to this article; see cruise reports by Carbotte *et al.*, 2012; Holbrook *et al.*, 2012). Data, experiment information, and ocean-bottom seismometer (OBS) instrument types were archived with the Marine Geoscience Data System (see Ⓔ Tables S1–S5). The first experiment MGL1211 was carried out from 14 June to 7 July 2012, including three main transects (lines 1–3), one short transect (line 4), three fan lines, and several short lines. The two ridge-perpendicular lines 1 and 2 extend from the JdF ridge to the Cascadia margin, covering the full width of the JdF plate. Line 3 starts ~10 km west of the Cascadia deformation front and runs parallel to the trench on the abyssal plain for a length of 400 km. Line 4 is located east of the axial seamount and oriented perpendicular to line 1. The second experiment

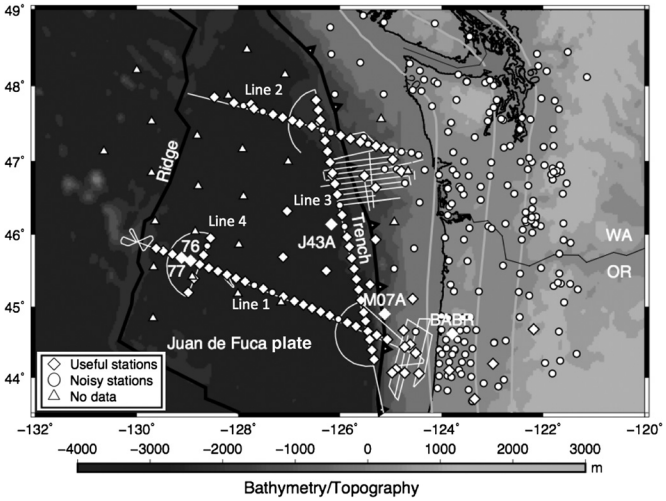

▲ **Figure 1.** Distribution of seismic stations and two active-source seismic experiments (thin white lines) used in this study. Diamond symbols represent seismic stations with clear air-gun shot recordings, and the circles represent stations with noisy data. Triangles represent the Cascadia Initiative offshore stations with no data recordings during the active-source expeditions. The large diamonds correspond to the seismic stations used in Figures 2, 3, 5, and 6. The depth contours of the Juan de Fuca plate interface from 20 to 60 km (gray lines) are from the model of McCrory *et al.* (2004). The thick black line represents the mid-ocean ridge.

MGL1212 was conducted on the continental shelf near the Grays Harbor area, Washington (dense white lines in Fig. 1), which started on 12 July 2012 and lasted for 12 days. This expedition included nine west–east transects from trench to margin and two north–south transects.

The volume of the air-gun arrays was kept constant (6600 cubic inches) throughout the two experiments, except for sequence 21 in MGL1211 and sequences 24 and 25 in MGL1212 (see Ⓔ Tables S3 and S4). We excluded those three sequences in our data analysis because of noisy first arrivals on data recordings. During MGL1211, the air-gun shots were triggered twice along lines 1–3, every 500 m for the refraction study and every 37.5 m for the multichannel seismic imaging study. The shot spacings for lines 2 and 4 are 37.5 and 150 m individually. The shot spacing was set as 170 m for the dense lines parallel to the trench near the continental shelf of central Oregon and a fan line west of the central Oregon trench. The source depth was set at 9 m for sequences 7–13 and 15–22 with a 15-s shot spacing, sequences 14 and 24–26 with a 60-s shot spacing, and sequences 23 and 27 with a 216-s shot spacing. For the rest of the sequences with 60- and 216-s shot spacings, the source depth was set at 12 m (see Ⓔ Table S3). During the MGL1212 experiment, the air-gun shot spacing and time interval remained nearly constant, 50 m and 23 s, respectively. The source depth of the air-gun array was set at 9 m for sequences 11–24, and 15 m for sequences 1–10 and 25,

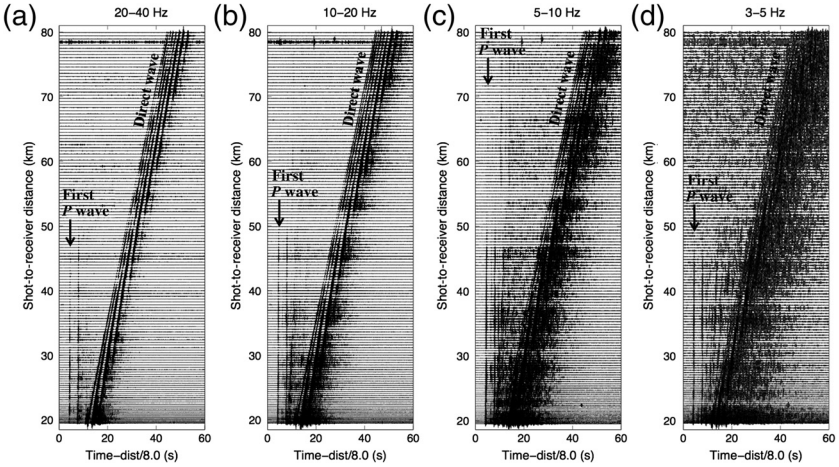

▲ **Figure 2.** Examples of the air-gun shot recordings by the Cascadia Initiative offshore station 7D.J43A on 15 June 2012, filtered at (a) 20–40 Hz, (b) 10–20 Hz, (c) 5–10 Hz, and (d) 3–5 Hz. The black arrow corresponds to the first *P*-wave arrivals at each frequency band. The average *P*-wave velocity for the direct-wave traveling in the water is 1.48 km/s. The *x* axis represents the reduced travel time with a reduction velocity of 8.0 km/s. See station location in Figure 1.

respectively (see Ⓔ Table S4). The deeper source depth was designated to enhance the data recording quality of the low-frequency content (J. Pablo Canales, personal comm., 2018).

In this study, we analyzed the air-gun shots of these two active-source experiments recorded by seismic instruments that were located around the experiment region. In total, we chose 114 offshore and 211 onshore stations (see station distribution in Fig. 1). These stations include the Cascadia Initiative seismic array (7D), Neptune Canada (NV), 47 OBSs deployed for MGL1211 (X6), complementary deployment of 40 temporary land stations in Oregon and Washington during the period of the active-source experiments (YG; Imaging the Cascadia subduction zone: A ship-to-shore opportunity). We also added many permanent and temporary land networks, including Cascade chain volcano monitoring network (CC), global seismograph network (IU), plate boundary borehole observatory seismic network (PB), EarthScope US Transportable Array (TA), University of Oregon regional network (UO), United States national seismic network (US), and Pacific Northwest regional seismic network (UW). Continuous vertical-component seismic data were requested during the expedition time (from 13 June to 24 July 2012) from the Incorporated Research Institutions for Seismology Data Management Center. The Cascadia Initiative deployed a total of 59 OBSs within the JdF plate during 2011–2012. However, only 31 were operating during the active-source experiments. The triangles in Figure 1 mark stations without seismic recordings.

We first explored the potential frequency ranges of each seismic station. The upper limit of frequency is defined by the Nyquist frequency, which is half of the sampling rate in the instrument. Among the 325 seismic stations, 80 have the BHZ component with a sampling rate of 40 or 50 samples per second, including part of networks 7D and UW and all stations from networks CC, IU, TA, UO, and US. The rest have either an HHZ or EHZ component with a sample rate equal to or greater than 100 samples per second, leading to a maximum upper limit of frequency greater than 50 Hz. Although the Nyquist frequency is up to 25 Hz for the BHZ stations and 50 Hz for the HHZ/EHZ stations, we only go up to 80% of the Nyquist frequency to remain conservative. Therefore, for the following data analysis, the seismic waveforms were filtered at multiple frequency bands, ranging from 3–5 Hz, 5–10 Hz, and 10–20 Hz for the BHZ stations and 3–5 Hz, 5–10 Hz, 10–20 Hz, and 20–40 Hz for the HHZ/EHZ stations.

No air-gun shot recordings can be easily detected from the raw seismic waveforms. To identify the air-gun shot signals, we made the common receiver gathering with a reduction velocity of 8.0 km/s for each seismic station from each active-source seismic transect. Our data analysis showed that the first *P*-wave arrivals can be clearly observed at many offshore stations up to 150 km away from the source within a broad range of frequency (see examples in Fig. 2 and Ⓔ Figs. S2–S5). Consistently, Horning *et al.* (2016) demonstrated similar maximum offset range of air-gun shot arrivals. It appears that stations located at deeper water recorded higher-frequency air-gun shot signals (Ⓔ Fig. S3) in comparison with stations located at shallower water (Ⓔ Figs. S4 and S5). The offshore stations also recorded strong direct waves, which travel through the water with an average *P*-wave velocity of 1.48 km/s. In total, we were able to identify clear air-gun shot recordings for 84 offshore instruments (diamonds in Fig. 1), including 7 from Lamont–Doherty Earth Observatory (LDEO), 20 from Woods Hole Oceanographic Institution (WHOI), 56 from Scripps Institution of Oceanography (SIO), and 1 from Neptune Canada (NV).

In contrast, only five land stations recorded clear air-gun shot signals up to 200 km away from the source, especially at 5–10 Hz (see examples in Fig. 3 and Ⓔ Figs. S6 and S7). All of these five stations were located in the remote areas of the Oregon fore-arc (diamonds in Fig. 1) and far away from possible human-made noise sources. In contrast, none of the stations located in the Washington remote areas showed clear air-gun shot recordings. The data quality difference between the Washington and Oregon stations may reflect the distinct structural variations along the Cascadia fore-arc. For example, the up-to-30-km sediment accumulations within the Olympic accretionary wedge in Washington (e.g., Calkins *et al.*, 2011; Calvert *et al.*, 2011; Rathnayaka and Gao, 2017) could significantly decrease the amplitude of the air-gun shot signals (e.g., Shulgin and Thybo, 2015). Furthermore, the thickened oceanic crust (25–35 km; Trehu *et al.*, 1994) and relatively low heat flow (< 40 mWm^{-2}; Ingebritsen and Mariner, 2010) in the Oregon fore-arc would allow

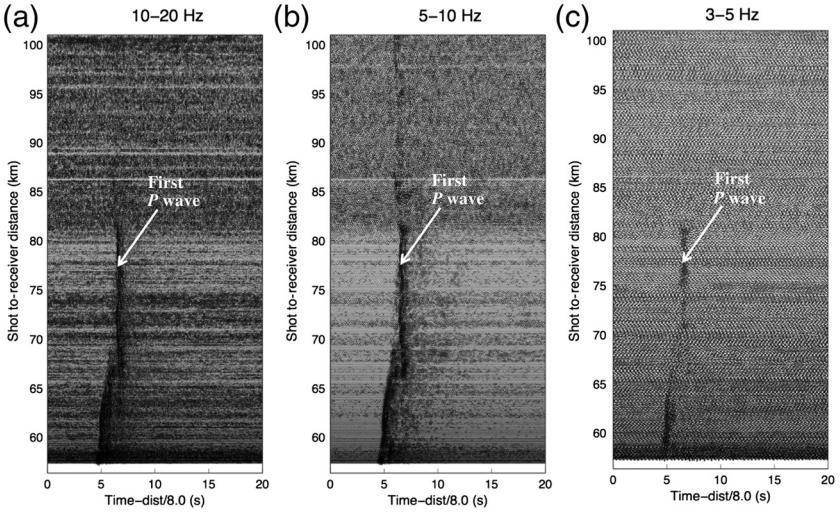

▲ **Figure 3.** Examples of the air-gun shot recordings by onshore station UW.BABR on 6 July 2012, filtered at (a) 10–20 Hz, (b) 5–10 Hz, and (c) 3–5 Hz. The white arrow corresponds to the first *P*-wave arrivals at each frequency band. The *x* axis represents the reduced travel time with a reduction velocity of 8.0 km/s. See station location in Figure 1.

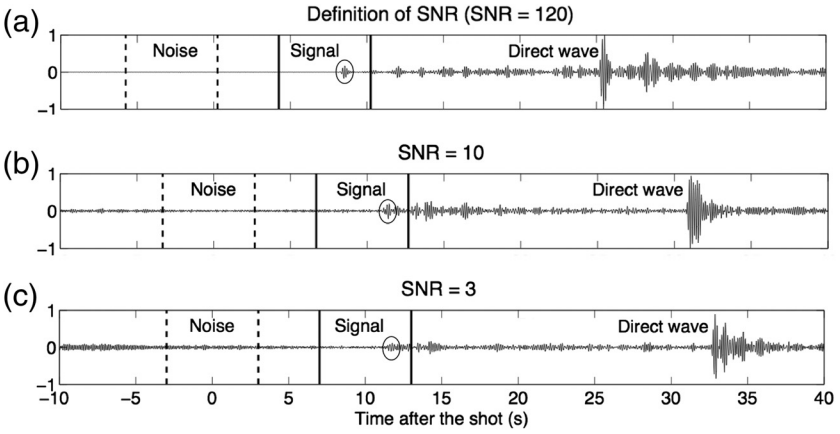

▲ **Figure 4.** Definition of the signal-to-noise ratio (SNR). (a) Example of air-gun shot recordings with SNR = 120. (b) Example of air-gun shot recordings with SNR = 10. (c) Example of air-gun shot recordings with SNR = 3. The seismic waveforms are filtered at 5–10 Hz. Solid and dashed lines define the 6-s signal window and the 6-s noise window, respectively. Black circles denote the first *P*-wave arrivals. The air-gun shot signal can be clearly observed at SNR ≥ 3.

propagation of seismic energy with less attenuation compared with thick sediments in the Washington fore-arc.

QUANTITATIVE ANALYSIS OF THE FIRST ARRIVALS

Hereinafter, we preceded the following data quality analysis only for the 89 seismic stations with signal-to-noise ratios (SNRs) ≥ 3 (the diamond symbols in Fig. 1). The signal is referred to as the maximum amplitude within the selected signal window (defined by an approximate velocity of 8 km/s), and the noise is defined as the standard deviation of the noise (see definition in Fig. 4). We chose a narrow 6-s signal window (4 and 2 s before and after the estimated phase arrival, respectively) to avoid interference with other phases. The noise window starts at 14 s before estimated first arrival for a total length of 6 s. Figure 4 shows that we can observe clear first arrivals with the SNR equal to or greater than 3.

The first *P* arrivals of the air-gun shot recordings can be either *Pg* (*P*-wave traveling in the crust) or head wave *Pn* (*P*-wave traveling in the uppermost mantle), which depends on the source-to-receiver distance. To distinguish these two phases, we applied a reduction velocity of 7.0 km/s for the common receiver gathering (Shillington *et al.*, 2004). We expect a positive trend between the phase arrival and the source-to-receiver distance for *Pg* and a negative trend for *Pn* (see examples in Fig. 5). We observed a transition of the first arrival from *Pg* to *Pn* at a source-to-receiver distance of about 25–40 km for offshore stations and 70–80 km for onshore stations.

We calculated and analyzed the SNR of the first *P* arrivals at multiple frequency bands for the seismic stations where the first *P* arrivals can be identified (SNR ≥ 3). The goal is to statistically and quantitatively investigate variations of the data quality in terms of source-to-receiver distance, frequency, air-gun shot depth and spacing, and site location. In general, the SNR decreases exponentially with increasing source-to-receiver distance at all the frequency ranges for both offshore and onshore stations (Figs. 6 and 7, and Ⓔ Fig. S8). This trend is expected considering the dissipation and attenuation of the seismic energy along the propagation path (e.g., Shulgin and Thybo, 2015). More specifically, at shorter distance, when *Pg* is the first arrival, the SNR varies within a large range, up to a few thousands for offshore stations (Figs. 6a–c and 7) and hundreds for land stations (Fig. 6d and Ⓔ Fig. S8). At longer distances, when *Pn* becomes the first arrival, the SNR on average is much smaller, < 300 and < 50 for offshore and land stations, respectively. The sharp decrease of the SNR near the *Pg*–*Pn* transition, as observed at many seismic stations, indicates that on average, the amplitude of the *Pn* phase is at least 10 times lower at offshore stations and 5 times lower at land stations than that of the *Pg* phase within our study region.

No general trend has been observed between the SNR variation and the frequency range. However, we noticed that the air-gun shot recordings at some deep-water stations

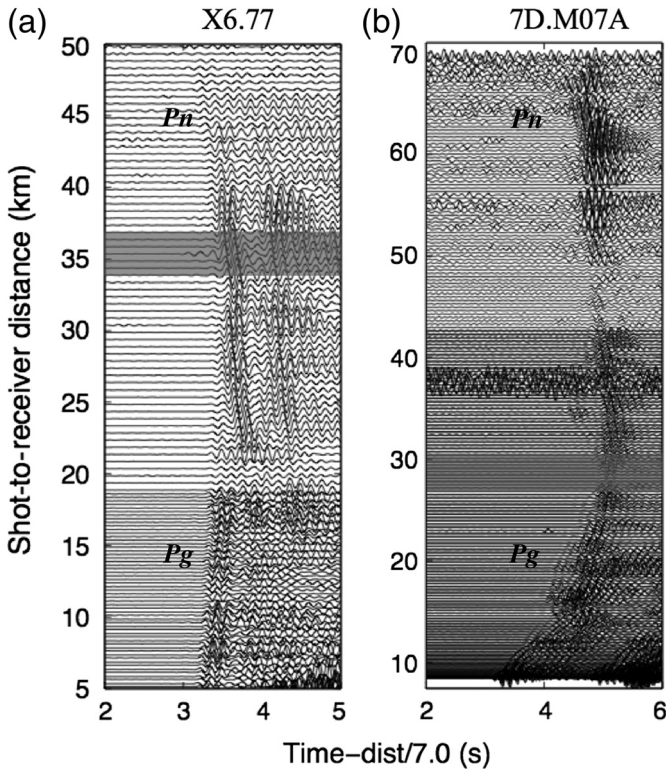

▲ **Figure 5.** Examples of the first *P*-wave arrivals for (a) deep-water seismic station X6.77 and (b) shallow-water station 7D.M07A. See station locations in Figure 1. The seismic waveforms are filtered at 5–10 Hz. The shaded area represents the phase transition from *Pg* to *Pn*. The *x* axis represents the reduced travel time with a reduction velocity of 7.0 km/s.

demonstrate relatively higher SNR values at 10–20 Hz than at 5–10 Hz (Fig. 6a). In contrast, for stations located near the trench or inland, the SNR decreases from 5–10 to 10–20 Hz (Fig. 6b–d). The SNR distribution from all the offshore stations with all the air-gun shots (Fig. 7) demonstrates similar patterns at 20–40, 10–20, and 5–10 Hz. The air-gun shot signals appear to be much noisier at 3–5 Hz, with the SNRs about 5–10 times lower than the ratios at higher frequencies. The SNR distribution from the five onshore stations suggests higher data quality at 5–10 Hz with SNR up to 250 than at 10–20 and 3–5 Hz where SNRs are less than 60 (Ⓔ Fig. S8).

We also explored the correlation of the data quality in terms of the source parameters. The SNR analysis shows that the data quality within our selected frequency range does not show strong dependence on the depth of the air-gun array (Fig. 8). For the MGL1211 experiment, we observed similar SNR variation pattern at source depths of 9 and 12 m, which decreases exponentially with increasing source-to-receiver distance (Fig. 8a). The SNR from MGL1212 does not vary much in terms of the shot-to-receiver distance at both source depths of 9 and 15 m and is 5–10 times lower than from MGL1211 (Fig. 8b). For MGL1211, we observed that the data recording quality increases with increasing shot spacing and time interval at all the frequencies (Fig. 8c). This indicates the direct effect of multiple waves from previous shots on the first *P*-wave arrivals of the air-gun shots.

ESTIMATE OF SEDIMENT THICKNESS

To estimate the sediment thickness beneath each offshore seismic station, we applied two types of layered models to best predict the observed *Pn* arrival time. A model with three layers above the oceanic mantle lithosphere, including water, sediment, and oceanic crust, is applied when the air-gun shot is located on the seaside of the trench (see model A in Fig. 9). A continental crustal layer is added between the oceanic sediment and the oceanic crust when both the source and the receiver are located between the trench and the continental margin (see model B in Fig. 9).

Equations (1) and (2) are used to estimate the sediment thickness for model A (Fig. 9b) and model B (Fig. 9c), respectively:

$$t = h_1\sqrt{\left(\frac{1}{v_1^2}-\frac{1}{v_5^2}\right)} + 2h_2\sqrt{\left(\frac{1}{v_2^2}-\frac{1}{v_5^2}\right)} + 2h_4\sqrt{\left(\frac{1}{v_4^2}-\frac{1}{v_5^2}\right)} + \frac{x}{v_5} \quad (1)$$

$$t = h_1\sqrt{\left(\frac{1}{v_1^2}-\frac{1}{v_5^2}\right)} + 2h_2\sqrt{\left(\frac{1}{v_2^2}-\frac{1}{v_5^2}\right)} + 2h_3\sqrt{\left(\frac{1}{v_3^2}-\frac{1}{v_5^2}\right)} + 2h_4\sqrt{\left(\frac{1}{v_4^2}-\frac{1}{v_5^2}\right)} + \frac{x}{v_5}, \quad (2)$$

in which t is the *Pn* arrival time and v_1–v_4 and h_1–h_4 correspond to *P*-wave velocities and layer thicknesses in water, sediment, continental crust, and oceanic crust, respectively. v_5 is the *P*-wave velocity in the uppermost mantle, and x is the shot-to-receiver distance.

The *P*-wave velocity in the water v_1 is set as 1.48 km/s, which matches well with the observed direct wave in this study. The selection of other model parameters is based on the recent work in Cascadia by Han *et al.* (2016, 2017), Horning *et al.* (2016), and Canales *et al.* (2017) (Fig. 9d). We assume a 6-km-thick oceanic crust (h_4) with the *P*-wave velocity (v_4) of 6.4 km/s. The *P*-wave velocities in the continental crust v_3 and uppermost mantle v_5 are set as 5.6 and 8.0 km/s, respectively. We used Gerdom *et al.* (2000) for the thickness of the continental crust layer h_3, which varies from trench toward the coastline. Variation of the water depth h_1 relies on the locations of the air-gun shot and the receiver.

As demonstrated by many previous studies (e.g., Han *et al.*, 2016; Horning *et al.*, 2016; Gomberg, 2018), the sediment thickness within the JdF plate varies within a broad range from the ridge to the accretionary wedge (≤ 5–6 km thick). The *P*-wave velocities of the oceanic sediment vary significantly within a range of 1.5–4.8 km/s, which increase gradually with

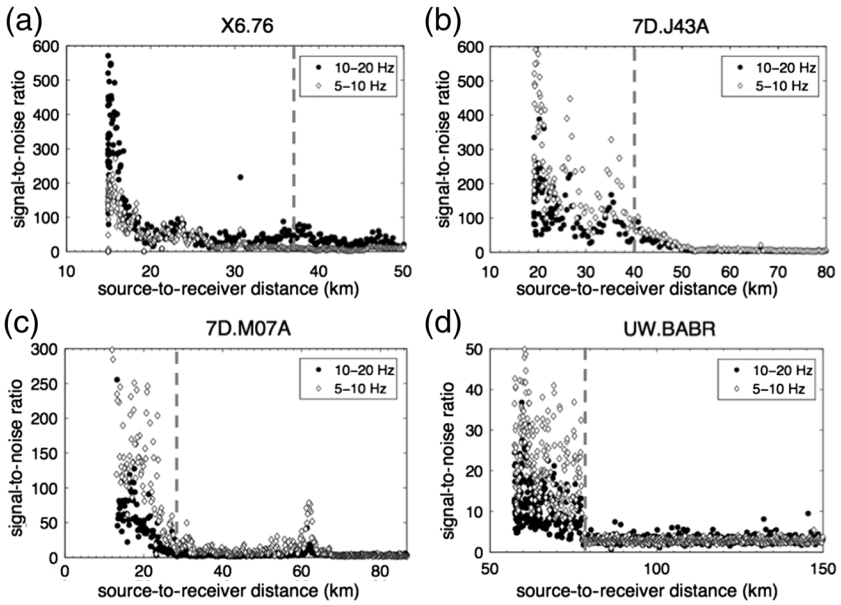

▲ **Figure 6.** Distribution of the SNR at individual stations. (a) SNR for offshore station X6.76 at deep water (2800 m), (b) SNR for offshore station 7D.J43A at water depth of 2654 m, (c) SNR for offshore station 7D.M07A at shallow water (1356 m), and (d) SNR for land station UW.BABR. See station locations in Figure 1. Black dots are measurements from 10 to 20 Hz, and open diamonds are from 5 to 10 Hz. The vertical dashed line represents the approximate phase transition from *Pg* to *Pn*.

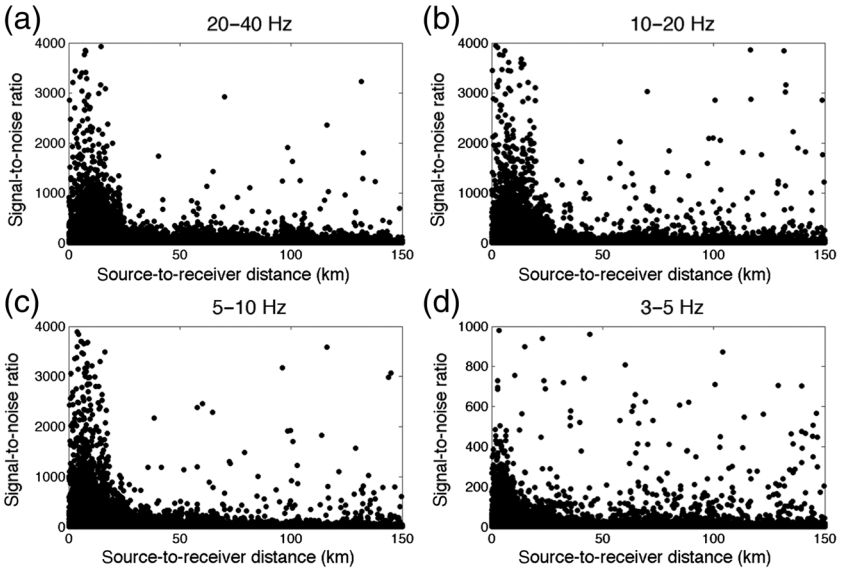

▲ **Figure 7.** Distribution of the SNR in terms of the source-to-receiver distance and frequency. The SNRs are from all the offshore stations with all the air-gun shot recordings, filtered at (a) 20–40 Hz, (b) 10–20 Hz, (c) 5–10 Hz, and (d) 3–5 Hz.

increasing sediment thickness (Han *et al.*, 2016, 2017; Horning *et al.*, 2016; Canales *et al.*, 2017). Therefore, we took variations of sedimentary velocities into consideration in our calculation of sediment thickness. The average velocities within the sediment layer (v_2) are set as 1.8 and 2.6 km/s, respectively. To minimize the ray-path effect on the estimate of sediment thickness h_2 beneath each receiver, we required the source-to-receiver distance within 35–50 km (Ⓔ Fig. S9). We then took the average of the estimated sediment thicknesses at the common receiver gatherings as the average sediment thickness beneath the station (Fig. 10).

DISTRIBUTION PATTERN OF SEDIMENT THICKNESS

Our estimated sediment thickness within the JdF plate is shown in Figure 10a (also see Ⓔ Fig. S10 and Table S6). The thickest sediment (3–5 km) is accumulated within the Cascadia accretionary wedge, consistent with many previous studies (e.g., Westbrook *et al.*, 1994; Flueh *et al.*, 1998; Goldfinger *et al.*, 2000; Scherwath *et al.*, 2006; Trehu *et al.*, 2006; Han *et al.*, 2016, 2017; Horning *et al.*, 2016; Gomberg, 2018). The sediment thickness is up to 4–5 km offshore the Oregon margin and within 3–3.5 km offshore the Washington margin, demonstrating significant along-strike variations. Unfortunately, because of uneven coverage of the seismic stations, we were unable to extract the sediment thickness distribution along the entire accretionary wedge.

In comparison with the active-source seismic results, we noticed that for receivers located near the deformation front and within the accretionary wedge, a 2.6 km/s sedimentary velocity could better predict the *Pn* arrivals. For receivers located further westward away from the deformation front, a 1.8 km/s sedimentary velocity fits the observations. For example, along line 3 of MGL1211, our estimated sediment thickness with a 2.6 km/s sedimentary velocity agrees well with the active-source seismic results by Canales *et al.* (2017) (< 200 m difference; Ⓔ Fig. S10d). Given a 1.8 km/s sedimentary velocity, we observed a tight agreement (i.e., < 150 m difference) of the sediment thickness between this study and Han *et al.* (2016) along line 2 of MGL1211 (Ⓔ Fig. S10c). The only exception is for the OBS located on the deformation front, where a 2.6 km/s sedimentary velocity matches better (the red dot in Ⓔ Fig. S10c). Along line 1, our sediment estimate at six sites, which are 75–150 km westward of the deformation front, is up to 800 m thicker than that of Horning *et al.* (2016; Ⓔ Fig. S10b). The discrepancy between our study and that of Horning *et al.* (2016) may be because of the trade-off between velocity and layer thickness. As shown by Horning *et al.* (2016), the *P*-wave velocities in

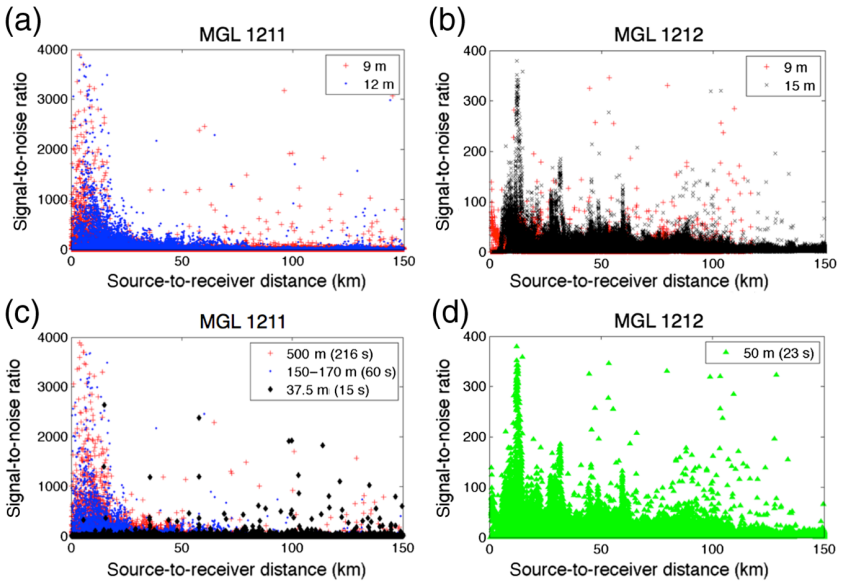

▲ **Figure 8.** Distribution of the SNR as a function of source parameters. (a) Comparison of the SNR at source depths of 9 m (pluses) and 12 m (dots) for MGL1211. (b) Comparison of the SNR at source depths of 9 m (pluses) and 15 m (crosses) for MGL1212. (c) Variation of the SNR in terms of the air-gun array spacing and time interval. Pluses, dots, and diamonds represent the 500 m, 150–170 m, and 37.5 m shot spacings for MGL1211, respectively. Data are filtered at 5–10 Hz. (d) Distribution of the SNR in terms of the air-gun array spacing and time interval for MGL1212. The color version of this figure is available only in the electronic edition.

the crust and upper mantle vary within a large range, from 4.5 to 7.5 km/s and from 6.5 to 8.5 km/s, respectively, and the crustal thickness varies from about 4.8 to 7.25 km. However, in our calculation, we simply used 6.4 and 8.0 km/s for the crust and mantle velocities, respectively, and a constant crustal thickness (6 km).

We also compared our estimated sediment thicknesses with the results by Bell *et al.* (2015) and Gomberg (2018; Ⓔ Fig. S11). For the four-shared sites by this study and Bell *et al.* (2015), our estimate of the sediment thickness is about 100–800 m thicker (Ⓔ Fig. S11a). The difference in the sediment thickness between this study and Gomberg (2018) varies from −1.1 km up to 2.6 km (Ⓔ Fig. S11b), which can be partly due to variations of sedimentary velocities. Gomberg (2018) defined the sediment thickness as the depth to *P*-wave velocity of 4.5 km/s. However, as demonstrated by active-source seismic results in Cascadia (Han *et al.*, 2016, 2017; Horning *et al.*, 2016; Canales *et al.*, 2017), the *P*-wave velocity is up to 4.8–5.0 km/s at the bottom of thick sediments.

To explore the impact of sediment thickness and water depth on data quality, we defined the average SNR at each seismic station as the average of all the SNR values from all the air-gun shots, filtered at 5–10 Hz, within a source-to-receiver distance between 25 and 45 km. For all types of instrumentations, the average SNR decreases from 26 to 8 with increasing sediment thickness (Fig. 10b) and from deep water to shallow water (Fig. 10c). Our analysis showed the highest SNR for the receivers located at deep-water column (~2800 m) and thin sediment coverage (~200 m). As described earlier (Fig. 8), we observed lower SNRs for the MGL1212 experiment in comparison with the MGL1211 experiment, which is mainly because that MGL1212 was located within the accretionary wedge where we observe the thickest sediments.

DISCUSSION AND CONCLUSIONS

We analyzed the data quality of the first *P*-wave arrivals from two active-source seismic experiments within the JdF plate, recorded by both offshore and onshore seismic stations. The common receiver gathering analysis showed that stations located in deep water recorded clear air-gun shot signals, but most stations located at shallow water appeared much noisier. We were able to identify air-gun shot seismic signals for only five land stations, which were all located within the Oregon fore-arc. The distribution of the SNR revealed a few general trends: (1) the ratio decreases with the increasing source-to-receiver distance, (2) the ratio increases from shallow to deep water, (3) the ratio decreases with the increasing thickness of the marine sediment and (4) the ratio decreases with the decreasing air-gun array spacing and time interval. We do not observe strong correlations between the data quality and the air-gun array depth.

It has been suggested by many previous active-source seismic studies that the air-gun shot signals can be largely affected by sediment thickness (e.g., Flueh *et al.*, 1998; Shillington *et al.*, 2004, 2008; Bohnenstiehl *et al.*, 2012). The thick sediments can attenuate the seismic energy (Tullos and Reid, 1969; Hamilton, 1972), resulting in relatively noisier data. Distinct low-velocity anomalies have been observed along the Cascade fore-arc at shallow depths (Rathnayaka and Gao, 2017), which were presumably related to sediments. Our quantitative and statistical analysis of the air-gun shot recordings further supports that the thick sediments within the accretionary wedge are the primary cause of the low SNR for stations located on the continental side of the trench. A few other factors may also contribute to the increased noise level at shallow-water and inland stations such as the interaction between oceanic waves with coastline, structural contrast across the continental margin, and a variety of human-made noise sources.

The sediment thickness estimated in this study increases from the ridge toward the continental margin, with significant along-strike variations. Recent seismic refraction studies (e.g., Trehu *et al.*, 2006; Han *et al.*, 2017) also showed significant decrease in sediment thickness (> 0.5 km) and increase in seafloor heat flow (up to 25 mWm^{-2}) from offshore Oregon northward to offshore Washington. Han *et al.* (2017) suggested that the along-strike variation of the sediment thickness within the accretionary wedge reflects the consolidation state of the

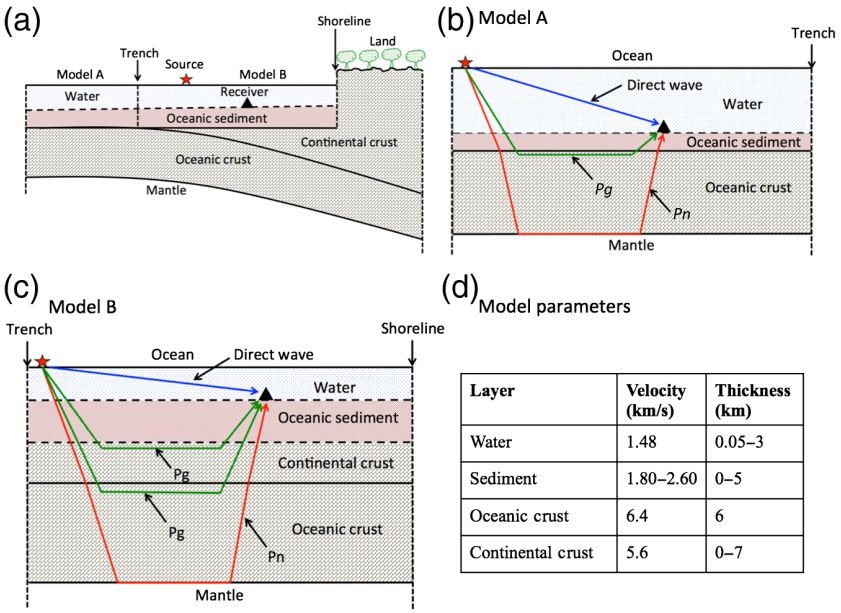

Layer	Velocity (km/s)	Thickness (km)
Water	1.48	0.05–3
Sediment	1.80–2.60	0–5
Oceanic crust	6.4	6
Continental crust	5.6	0–7

▲ **Figure 9.** Simplified layered models used to predict the arrival time of the first *P* waves. (a) Schematic diagram of the subduction zone. The star represents the air-gun shot location and the triangle for the receiver location. (b) A simple three-layer model for the case when the air-gun shot is located on the seaside of the trench. (c) A continental crustal layer is added between the oceanic sediment and the oceanic crust when both the source and the receiver are located between the trench and the coastline. (d) Model parameters within each layer based on Gerdom *et al.* (2000), Han *et al.* (2016, 2017), and Horning *et al.* (2016). The layer thickness depends on the actual locations of the source and the receiver. The color version of this figure is available only in the electronic edition.

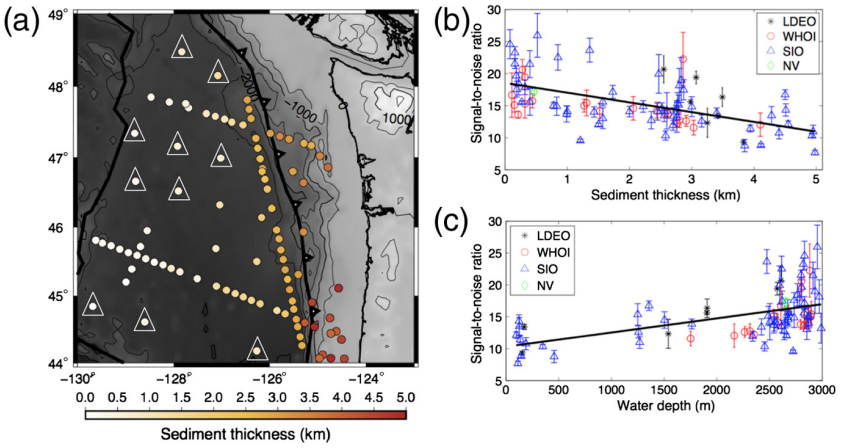

▲ **Figure 10.** (a) Distribution of sediment thickness estimated beneath each offshore seismic station. Triangles represent the Cascadia Initiative stations with no data recordings during the active-source expeditions, and the sediment thickness beneath these stations is obtained from Bell *et al.* (2015). (b) Variation of the average SNR in terms of sediment thickness. (c) Variation of the average SNR in terms of water depth. In (b,c), stars, circles, triangles, and diamonds represent Lamont–Doherty Earth Observatory (LDEO), Woods Hole Oceanographic Institution (WHOI), Scripps Institution of Oceanography (SIO), and Neptune Canada (NV) instruments, respectively. Black solid lines represent the best linear fits for the data. The color version of this figure is available only in the electronic edition.

sediments. The thick sediment accumulation acts as a thermally resistive blanket, which increases the basement temperature and prevents heat conduction through sediment to the ocean floor (e.g., Davis *et al.*, 1999; Trehu *et al.*, 2006; Salmi *et al.*, 2017). We did not observe a strong correlation between variations of the sediment thickness and the gravity anomalies (e.g., Wells *et al.*, 2003; Blakely *et al.*, 2005; Sandwell *et al.*, 2013), which may be partly because of the influence of the accreted Siletz oceanic terrane (Blakely *et al.*, 2005).

The sediment within the Oregon accretionary wedge is up to 5 km thick, where the highest fault slip was predicted for the great A.D. 1700 Cascadia earthquake (Wang *et al.*, 2013) and a higher locking rate (up to 40 mm/yr) on the Cascadia megathrust was obtained (Pollitz and Evans, 2017; see Ⓔ Fig. S12a). The spatial correlation may imply the influence of the Cascadia megathrust earthquake and seamount subsidence on the redistribution of sediments along strike. More broadly, the region where we observed relatively thick sediments within the southern JdF plate corresponds with the distribution of small earthquakes (magnitudes ≤ 4) within and above the JdF slab (Ⓔ Fig. S12b). The seismicity on the seaside of the trench was attributed to hydration of the downgoing oceanic plate and reactivation of pre-existing faults (Han *et al.*, 2016; Horning *et al.*, 2016). Here, in terms of the coincidence of our sediment distribution with observed seismicity, we suggest that the thick and less consolidated sediment accumulation offshore Oregon may play a significant role on the coupling of the plate interface (e.g., Heuret *et al.*, 2012).

Our analysis of the air-gun shot recordings provides very useful 3D seismic datasets within the entire JdF plate. This is particularly important for the model resolution within the oceanic crust and the uppermost mantle. As well known, seismic tomographic studies with different types of datasets are complementary to each other but are usually carried out separately, leaving a gap in the model resolution. The active-source seismic recordings have been successfully applied to study the shallow crustal structures both onshore and offshore. Regional body-wave tomography provides strong constraints on the upper-mantle structure, and surface-wave tomography is well suited to resolve structures from the crust down to ~200 km depth. Integration of high-frequency air-gun shots and short-period surface waves will provide a tight constraint of the structure from the shallowest sedimentary layers down to tens of kilometers,

filling the gap in the model resolution between active- and passive-source seismic tomographic images.

DATA AND RESOURCES

Seismic data used in this study were obtained from the Incorporated Research Institutions for Seismology (IRIS) Data Management Center (https://ds.iris.edu/mda, last accessed August 2018). Information about the seismic reflection and refraction experiments were obtained from the Marine Geoscience Data System (http://www.marine-geo.org/index.php, last accessed August 2018).

ACKNOWLEDGMENTS

This research was supported by the National Science Foundation (Grant Number EAR-1635903) and the startup support of H. Gao at the University of Massachusetts Amherst. The authors thank Shuoshuo Han and Juan Pablo Canales for the thoughtful discussions about the cruise information of the MGL1211 active-source seismic experiment and the interpretation of the air-gun shot seismic recordings. The authors thank Juan Pablo Canales for providing the seismic velocity profiles along lines 1 and 3 for MGL1211. The authors thank the associate editor and two anonymous reviewers for their comments and suggestions.

REFERENCES

Bell, S. W., Y. Ruan, and D. W. Forsyth (2015). Shear velocity structure of abyssal plain sediments in Cascadia, *Seismol. Res. Lett.* **86,** no. 5, 1247–1252.

Bilek, S. L. (2009). Seismicity along the South American subduction zone: Review of large earthquakes, tsunamis, and subduction zone complexity, *Tectonophysics* **495,** nos. 1/2, 2–14, doi: 10.1016/j.tecto.2009.02.037.

Blakely, R. J., T. M. Brocher, and R. E. Wells (2005). Subduction-zone magnetic anomalies and implications for hydrated forearc mantle, *Geology* **33,** no. 6, 445–448, doi: 10.1130/G21447.1.

Bleibinhaus, F., J. A. Hole, T. Ryberg, and G. S. Fuis (2007). Structure of the California Coast ranges and San Andreas fault at SAFOD from seismic waveform inversion and reflection imaging, *J. Geophys. Res.* **112,** no. B6, doi: 10.1029/2006JB004611.

Bohnenstiehl, D. R., C. M. Scheip, H. Matsumoto, and R. P. Dziak (2012). Acoustics variability of air gun signals recorded at intermediate ranges within the Lau Basin, *Geochem. Geophys. Geosys.* **13,** no. Q11013, doi: 10.1029/2012GC004337.

Calkins, J. A., G. A. Abers, G. Ekstrom, K. C. Creager, and S. Rondenay (2011). Shallow structure of the Cascadia subduction zone beneath western Washington from spectral ambient noise correlation, *J. Geophys. Res.* **116,** no. B07302, doi: 10.1029/2010JB007657.

Calvert, A. J., L. A. Preston, and A. M. Farahbod (2011). Sedimentary underplating at the Cascadia mantle-wedge corner revealed by seismic imaging, *Nature Geosci.* **4,** 545–548, doi: 10.1038/NGEO1195.

Canales, J. P., S. M. Carbotte, M. R. Nedimivic, and H. Carton (2017). Dry Juan de Fuca slab revealed by quantification of water entering Cascadia subduction zone, *Nature Geosci.* **10,** 864–872.

Carbotte, S., P. Canales, H. Carton, and M. Nedimovic (2012). Juan de Fuca plate: Ridge to trench, *Cruise Report*, available at http://www.marine-geo.org/tools/search/entry.php?id=MGL1211 (last accessed August 2018).

Christeson, G. L., H. J. A. Van Avendonk, S. P. S. Gulick, R. S. Reece, G. L. Pavlis, and T. L. Pavlis (2013). Moho interface beneath Yakutat terrane, southern Alaska, *J. Geophys. Res.* **118,** no. 9, 5084–5097.

Dash, R., and G. Spence (2011). *P*-wave and *S*-wave velocity structure of northern Cascadia margin gas hydrates, *Geophys. J. Int.* **187,** no. 3, 1363–1377.

Davis, E. E., D. S. Chapman, K. Wang, H. Villinger, A. T. Fisher, S. W. Robinson, J. Grigel, D. Pribnow, J. Stein, and K. Becker (1999). Regional heat flow variations across the sedimented Juan de Fuca ridge eastern flank: Constraints on lithospheric cooling and lateral hydrothermal heat transport, *J. Geophys. Res.* **104,** no. B8, 17,675–17,688.

Flueh, E. R., M. A. Fisher, J. Bialas, J. R. Childs, D. Klaeschen, N. Kukowski, T. Parson, D. W. Scholl, U. ten Brink, A. M. Trehu, *et al.* (1998). New seismic images of the Cascadia ubduction zone from cruise SO108-ORWELL, *Tectonophysics* **293,** 69–84.

Funck, T., K. E. Louden, R. J. Wardle, J. Hall, J. W. Hobro, M. H. Salisbury, and A. M. Muzzatti (2000). Three-dimensional structure of the Torngat Orogen (NE Canada) from active seismic tomography, *J. Geophys. Res.* **105,** no. B10, 23,403–23,420.

Gerdom, M., A. M. Trehu, E. R. Flueh, and D. Klaeschen (2000). The continental margin off Oregon from seismic investigations, *Tectonophysics* **329,** nos. 1/4, 79–97, doi: 10.1016/S0040-1951(00)00190-6.

Goldfinger, C., L. D. Kulm, L. C. Mcneill, and P. Watts (2000). Superscale failure of the southern Oregon Cascadia margin, *Pure Appl. Geophys.* **157,** 1189–1226.

Gomberg, J. (2018). Cascadia onshore–offshore site response, submarine sediment mobilization, and earthquake recurrence, *J. Geophys. Res.* **123,** 1381–1404, doi: 10.1002/2017JB014985.

Guo, Y., K. Koketsu, and H. Miyake (2016). Propagation mechanism of long-period ground motions for offshore earthquakes along the Nankai trough: Effects of the accretionary wedge, *Bull. Seismol. Soc. Am.* **106,** no. 3, 1176–1197, doi: 10.1785/0120150315.

Hamilton, E. L. (1972). Compressional-wave attenuation in marine sediments, *Geophysics* **37,** no. 4, 620–646.

Han, S., N. L. Bangs, S. M. Carbotte, D. M. Saffer, and J. C. Gibson (2017). Link between sediment consolidation and Cascadia megathrust slip behavior, *Nature Geosci.* **10,** 954–959.

Han, S., S. M. Carbotte, J. P. Canales, M. R. Nedimovic, H. Carton, J. C. Gibson, and G. W. Horning (2016). Seismic reflection imaging of the Juan de Fuca plate from ridge to trench: New constraints on the distribution of faulting and evolution of the crust prior to subduction, *J. Geophys. Res.* **121,** no. 3, 1849–1872.

Heuret, A., C. P. Conrad, F. Funiciello, S. Lallemand, and L. Sandri (2012). Relation between subduction megathrust earthquakes, trench sediment thickness and upper plate strain, *Geophys. Res. Lett.* **39,** no. 5, doi: 10.1029/2011GL050712.

Holbrook, W. S., G. M. Kent, K. Keranen, A. Trehu, and P. Johnson (2012). Cascadia open access seismic transects (COAST), *Cruise Report*, available at http://www.marine-geo.org/tools/entry/MGL1212 (last accessed August 2018).

Horning, G., J. P. Canales, S. M. Carbotte, S. Han, H. Carton, M. R. Nedimovic, and P. E. van Keken (2016). A 2-D tomographic model of the Juan de Fuca plate from accretion at axial seamount to subduction at the Cascadia margin from an active source ocean bottom seismometer survey, *J. Geophys. Res.* **121,** 5859–5879.

Ingebritsen, S. E., and R. H. Mariner (2010). Hydrothermal heat discharge in the Cascade Range, northwestern United States, *J. Volcanol. Geoth. Res.* **196,** 208–218, doi: 10.1016/j.jvolgeores.2010.07.023.

Johnson, H. P., J. Gomberg, S. L. Hautala, and M. S. Salmi (2017). Sediment gravity flows triggered by remotely generated earthquake waves, *J. Geophys. Res.* **122,** 4584–4600, doi: 10.1002/2016JB013689.

McCaffrey, R., A. I. Qamar, R. W. King, R. Wells, G. Khazaradze, C. A. Williams, C. W. Stevens, J. J. Vollick, and P. C. Zwick (2007). Fault locking, block rotation and crustal deformation in the Pacific

Northwest, *Geophys.J. Int.* **169,** no. 3, 1315–1340, doi: 10.1111/j.1365-246X.2007.03371.x.
McCrory, P. A., J. L. Blair, D. H. Oppenheimer, and S. R. Walter (2004). Depth to the Juan de Fuca slab beneath the Cascadia subduction margin: A 3-D model for sorting earthquakes, *U.S. Geol. Surv. Data Ser. DS-91*.
Phrampus, B. J., R. N. Harris, and A. M. Trehu (2017). Heat flow bounds over the Cascadia margin derived from bottom simulating reflectors and implications for thermal models of subduction, *Geochem. Geophys. Geosys.* **18,** 3309–3326, doi: 10.1002/2017GC007077.
Pollitz, F. F., and E. L. Evans (2017). Implications of the earthquake cycle for inferring fault locking on the Cascadia megathurst, *Geophys. J. Int.* **209,** 167–185.
Rathnayaka, S., and H. Gao (2017). Crustal-scale seismic structure from trench to forearc in the Cascadia subduction zone, *J. Geophys. Res.* **122,** 7311–7328.
Ruan, Y., D. W. Forsyth, and S. W. Bell (2014). Marine sediment shear velocity structure from the ratio of displacement to pressure of Rayleigh waves at seafloor, *J. Geophys. Res.* **119,** no. 8, 6357–6371.
Salmi, M. S., H. P. Johnson, and R. N. Harris (2017). Thermal environment of the Southern Washington region of the Cascadia subduction zone, *J. Geophys. Res.* **122,** 5852–5870, doi: 10.1002/2016JB013839.
Sandwell, D. T., E. Garcia, K. Soofi, P. Wessel, and W. H. F. Smith (2013). Towards 1 mGal global marine gravity from CryoSat-2, Envisat, and Jason-1, *The Leading Edge* **32,** no. 8, 892–899, doi: 10.1190/tle32080892.1.
Scherwath, M., M. Riedel, G. D. Spence, and R. D. Hyndman (2006). Data report: Seismic structure beneath the northern Cascadia drilling transect of IODP Expedition 311, *Proc. IODP*, Vol. 311, 25 pp.
Shillington, D. J., H. J. A. Van Avendonk, W. S. Holbrook, P. B. Kelemen, and M. J. Hornbach (2004). Composition and structure of the central Aleutian island arc from arc-parallel wide-angle seismic data, *Geochem. Geophys. Geosys.* **5,** no. Q10006, doi: 10.1029/2004GC000715.
Shillington, D. J., T. A. Minshull, C. Peirce, and J. M. O'sullivan (2008). *P* and *S* wave velocities of consolidated sediments from a seafloor seismic survey in the North Celtic sea basin, offshore Ireland, *Geophys. Prospect.* **56,** no. 2, 197–211.
Shulgin, A., and H. Thybo (2015). Seismic explosion sources on an ice cap—Technical considerations, *Polar Sci.* **9,** 107–118.
Song, T. A., and M. Simons (2003). Large trench-parallel gravity variations predict seismogenic behavior in subduction zones, *Science* **301,** 630.
Stephenson, W. (2007). Velocity and density models incorporating the Cascadia subduction zone for 3D earthquake ground motion simulations, *U.S. Geol. Surv. Open-File Rept. 2007-1348*, 1–28 pp.
Sumy, D. F., J. A. Lodewyk, R. L. Woodward, and B. Evers (2015). Ocean-bottom seismograph performance during the Cascadia initiative, *Seismol. Res. Lett.* **86,** no. 5, 1238–1246.
Trehu, A. M., I. Asudeh, T. M. Brocher, J. H. Luetgert, W. D. Mooney, J. L. Nabelek, and Y. Nakamura (1994). Crustal architecture of the Cascadia forearc, *Science* **266,** 237–243, doi: 10.1126/science.266.5183.237.
Trehu, A. M., R. J. Blakely, and M. C. Williams (2012). Subducted seamounts and recent earthquakes beneath the central Cascadia forearc, *Geology* **40,** no. 2, 103–106.
Trehu, A. M., M. E. Torres, G. Bohrmann, and F. S. Colwell (2006). Leg 204 synthesis: Gas hydrate distribution and dynamics in the central Cascadia accretionary complex, *Proc. ODP: Sci. Results*, Vol. 204, 40 pp.
Tullos, F. N., and A. C. Reid (1969). Seismic attenuation of gulf coast sediments, *Geophysics* **34,** no. 4, 516–528.
Wallace, L. M., R. Bell, J. Townend, S. Ellis, S. Bannister, S. Henrys, R. Sutherland, and P. Barnes (2010). Subduction systems revealed: Studies of the Hikurangi margin, *Eos Trans. AGU* **91,** no. 45, 417–428.
Wang, K., and A. M. Trehu (2016). Invited review paper: Some outstanding issues in the study of great megathrust earthquakes—The Cascadia example, *J. Geodyn.* **98,** 1–18.
Wang, P.-L., S. E. Engelhart, K. Wang, A. D. Hawkes, B. P. Horton, A. R. Nelson, and R. C. Witter (2013). Heterogeneous rupture in the great Cascadia earthquake of 1700 inferred from coastal subsidence estimates, *J. Geophys. Res.* **118,** 2460–2473, doi: 10.1002/jgrb.50101.
Wells, R. E., R. J. Blakely, Y. Sugiyama, D. W. Scholl, and P. A. Dinterman (2003). Basin-centered asperities in great subduction zone earthquakes: A link between slip, subsidence, and subduction erosion?, *J. Geophys. Res.* **108,** no. B10, 2507.
Westbrook, G. K., B. Carson, and R. J. Musgrave (1994). Leg 146 introduction: Cascadia margin, *Proc. ODP: Init. Repts.*, Vol. 146 (part 1).

APPENDIX

We analyzed the frequency spectrum of a day-long recording for both onshore and offshore stations to diagnose the diurnal effect of the background noise. Preliminary noise analysis of the Cascadia Initiative showed that the power spectra are relatively independent of water depth but demonstrate seasonal dependence to some extent (Sumy *et al.*, 2015). Based on the cruise reports (Carbotte *et al.*, 2012; Holbrook *et al.*, 2012), the UTC midnight is equal to 17:00 local time. Our analysis demonstrated that the frequency spectrogram of offshore stations shows similar patterns for daytime and nighttime; in comparison, some land stations show strong diurnal variations on a broad frequency range. We used the Lamont–Doherty

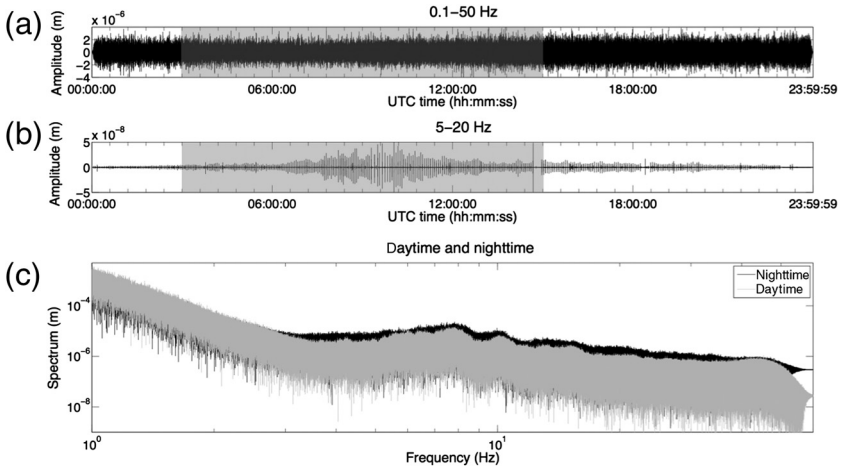

▲ **Figure A1.** Analysis of day-long frequency spectrogram for the Lamont–Doherty Earth Observatory trawl-resistant offshore station 7D.FN14A. See station location in Ⓔ Figure S1, available in the electronic supplement to this article. (a) Raw seismic waveforms without filtering. (b) The seismic waveforms are filtered at 5–20 Hz. (c) The frequency spectrum for daytime (gray) and nighttime (black). The gray-shaded segments of the seismic waveforms in (a,b) represent the 03:00–15:00 UTC nighttime.

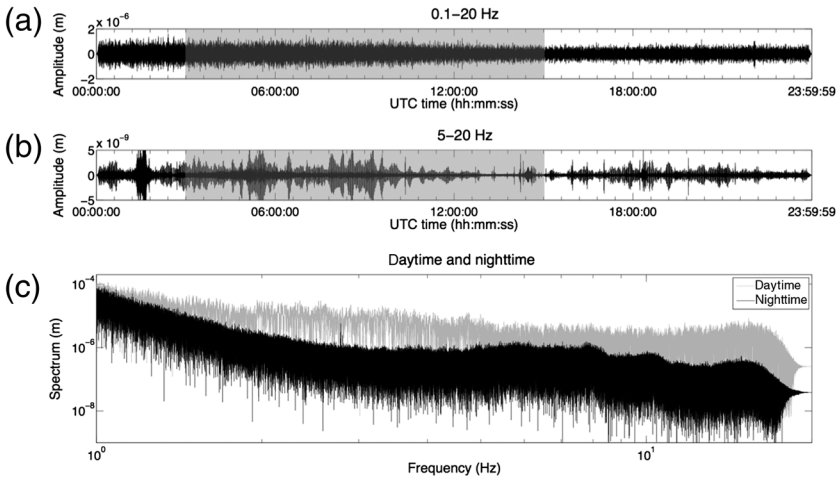

▲ **Figure A2.** Analysis of day-long frequency spectrogram for the EarthScope Transportable Array station TA.I02D. See station location in Ⓔ Figure S1. (a) Raw seismic waveforms without filtering. (b) The seismic waveforms are filtered at 5–20 Hz. (c) The frequency spectrum for daytime (gray) and nighttime (black). The gray-shaded segments of the seismic waveforms in (a,b) represent the 03:00–15:00 UTC nighttime.

Earth Observatory trawl-resistant offshore station 7D.FN14A and the land station TA.I02D as examples (see station locations in Ⓔ Fig. S1, available in the electronic supplement to this article). The raw day-long seismic recordings by both stations show no temporal variations (Figs. A1a and A2a). For station 7D.FN14A, we observed the air-gun shot arrivals, which appear as numerous strong signals (about 5–200 times of the background noise level) at periodic intervals after filtering the seismic recordings between 5 and 20 Hz (Fig. A1b). The frequency spectrogram appears similar during daytime and nighttime (Fig. A1c, gray and black lines). The strong signals within 3 Hz may correspond to the background noise level, and the relatively high-seismic energy at 3–20 Hz reflects the air-gun shots. In contrast, the seismogram by station TA.I02D, which is located in a highly populated area, appears to be much noisier. The nighttime frequency spectrogram at TA.I02D (Fig. A2c) shows a similar pattern as the daytime/nighttime spectrogram at 7D.FN14A. The magnitude of the frequency spectrogram is much stronger during daytime (15:00–03:00 UTC time/8:00–20:00 local time; Fig. A2c, gray lines) compared with the quiet nighttime (03:00–15:00 UTC time/20:00–8:00 local time; Fig. A2c, black lines).

Sampath Rathnayaka
Haiying Gao
Department of Geosciences
University of Massachusetts Amherst
627 North Pleasant Street
Amherst, Massachusetts 01003 U.S.A.
srathnayakam@geo.umass.edu

Published Online 14 November 2018